



Budapest University of Technology and Economics  
Faculty of Electrical Engineering and Informatics  
Department of Electron Devices

---

# **Modelling and Optimization of Hybrid Photovoltaic- Thermoelectric Generator Systems for Electrical Energy Generation**

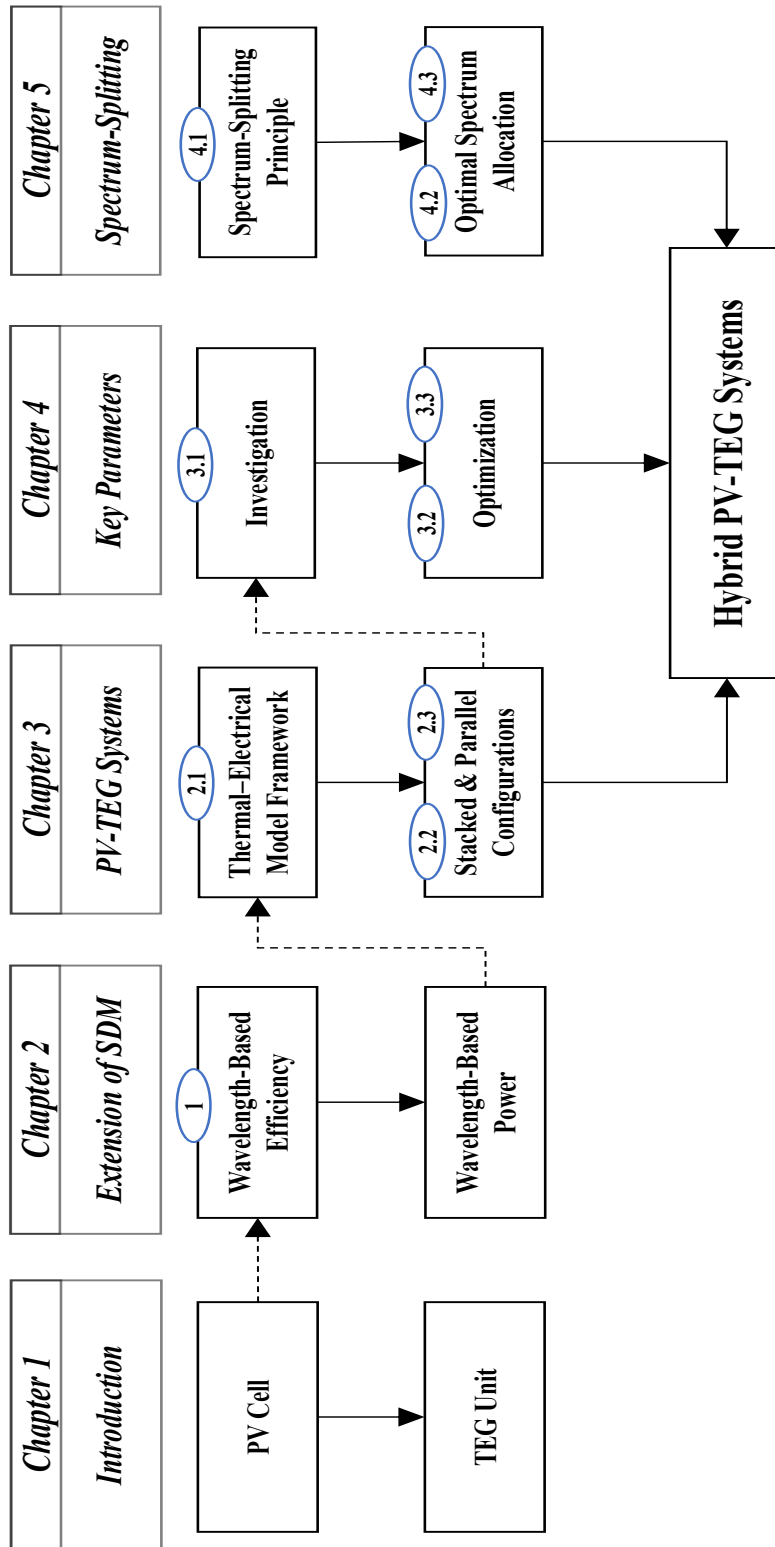
---

Ph.D. Thesis Booklet

**Ahmed I. M. Alnahhal**

Thesis supervisor:  
**Balázs Plesz, Ph.D.**

Budapest  
2026



# 1 Introduction and motivation

Photovoltaic (PV) solar cells have emerged as one of the most viable solutions for converting solar energy into electrical power [1]. This means generating an electric current without any moving parts or emissions.

Despite the considerable progress in the development of solar cells, several constraints continue to impede their PCE. The operational limitations have a high-scale effect on the PCE of the solar cells. The critical operational limitations are deeply rooted in the fundamental operating principles of solar cells. **First**, only photons with energy equal to or just higher than the bandgap energy of the solar cell material can generate an electron-hole pair within the PV cell. Consequently, solar cells utilize only a portion of the solar spectrum, while photons with energy lower than the bandgap energy are absorbed as heat (Post-Bandgap Losses). **Second**, the bandgap of a semiconductor material sets the maximum energy of photons that have the ability to generate an electron-hole pair. Only energy equaling the band gap can be extracted from each above-bandgap photon, particularly the high-energy photons, while excess energy thermalizes into heat (Thermalization Losses). Fig. 1.1 illustrates the problem statement and outlines the key factors limiting the power conversion efficiency of single junction silicon solar cells.

Thermoelectric generators (TEGs) represent a promising technology for direct energy conversion, transforming thermal energy into electrical energy through the Seebeck effect. TEGs possess several unique characteristics that distinguish them from conventional energy conversion technologies, including high reliability and minimal moving parts [2]. Since its initial discovery, thermoelectric technology has evolved considerably, with major advancements in materials science and semiconductor engineering [3].

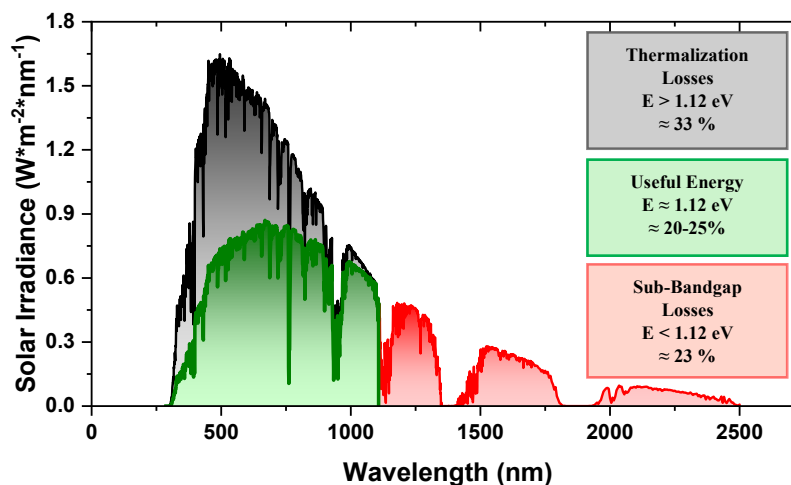


Fig. 1.1 The summary of the problem statement.

## 2 Objectives

The key research contribution focuses on integrating a TEG unit with a PV cell, thereby overcoming the limitations of the standalone single junction PV cell, and achieving higher overall efficiency. This involves introducing different hybrid PV-TEG configurations for addressing the different types of losses and recovering the waste heat of single-junction solar cells. In addition, optimizing the key parameters to maximize overall efficiency.

### 2.1 Thesis 1

Despite the frequent studies that grasp how the PV cells behave at different spectral conditions, the traditional SDM overlooks the spectral dependence of the incoming solar radiation. This limits their ability to accurately represent the complex interaction between the solar cells and the incoming light spectrum. This thesis aims to bridge this gap by investigating the effect of spectrum wavelengths on the output performance of different solar cells, i.e., different semiconductor materials under different solar spectra. The study focuses on extending the SDM by incorporating a spectral sensitivity into the photo-generated current [j1]. In addition, it introduces the concept of wavelength-dependent efficiency for calculating overall efficiency under the different solar spectra [c5]. This metric offers insights into potential strategies for spectrum-specific optimization of solar cell designs, such as tandem solar cells and hybrid PV-TEG systems.

### 2.2 Thesis 2

The literature states that single-technology approaches often fail to capture the full potential of solar energy. The development of hybrid energy systems has been driven by the limitations of standalone systems and the need for innovative solutions to enhance energy utilization [4]. However, achieving optimal performance requires a thorough understanding of their configurations, interaction mechanisms between the two devices, and performance metrics [c3] [c4]. This thesis is built on existing research to provide a comprehensive comparative analysis of stacked and parallel configurations, focusing on their thermal-electrical interaction dynamics at various light concentration levels [c1], providing a foundation for evaluating their performance through modeling and comparative discussion [j2]. This offers insights into optimizing their design and performance, paving the way for broader applications in sustainable energy solutions.

### 2.3 Thesis 3

The main objective is to improve the performance of the hybrid PV-TEG systems through a comprehensive investigation and optimization of key parameters that significantly influence the efficiency of the PV cell and TEG subsystem [j2]. This thesis explores how key parameters influence thermal and electrical performance. In addition, focuses on developing optimization strategies that can maximize conversion efficiency, minimize thermal losses, and provide insight for more efficient designs [c2]. Moreover, this thesis seeks to unravel the complex relationships between these parameters, offering a comprehensive framework to understand and improve the operational characteristics of the hybrid PV-TEG systems that can support future research.

### 2.4 Thesis 4

While the basic splitting spectrum approach has shown improvements in the overall conversion efficiency compared to the stacked configuration, it may not represent the optimal utilization of the solar spectrum [c3]. This thesis aims to determine the optimal spectrum splitting configuration for maximizing overall efficiency by further splitting the within-bandgap spectrum and selectively distributing portions between the PV and TEG subsystems [j3]. This is attributed to several observations. First, photons with energy significantly exceeding the bandgap of the Si lead to thermalization losses in the PV cells, where excess energy is converted to heat rather than electrical energy. Second, the TEG subsystem operates at higher temperature gradients, leading to higher conversion efficiency.

## 3 Methodology

### 3.1 Extension of SDM of Solar Cells for Spectral Sensitivity Under Different Solar Spectra

The study focuses on extending the SDM of single junction solar cells to the spectrum sensitivity by introducing a spectral dependence into the photo-generated current ( $I_{ph}$ ), as seen in Fig. 3.1 [j3]. This allows for designing an applicable wavelength-based efficiency model of solar cells using readily available datasheet parameters, specifically, the current-voltage ( $I - V$ ) characteristics and external quantum efficiency ( $EQE$ ).

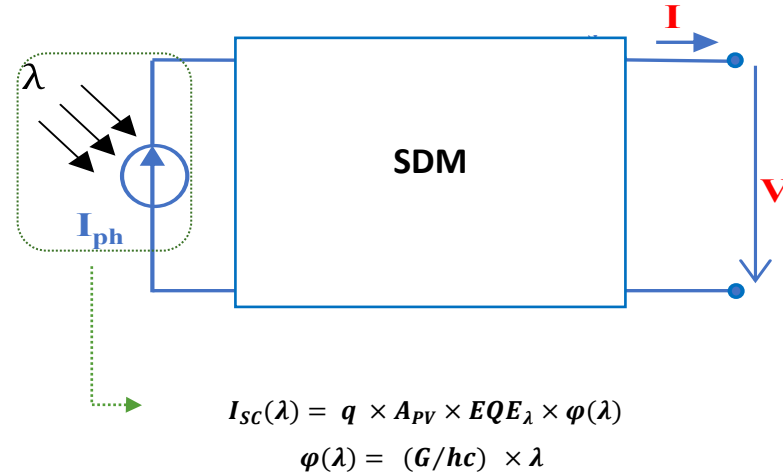


Fig. 3.1 Spectral sensitivity to the photo-generated current

The full wavelength spectrum of AM0 and AM1.5G the solar spectra is segmented into discrete wavelengths in a specific step for both the ideal and real solar cells. To ensure the readability and clarity of the ( $I - V$ ) and power-voltage ( $P - V$ ) curves, the corresponding spectrum is partitioned into a limited number of wavelengths that effectively illustrate the results. The proposed spectrum partitioning of the ideal solar cells is made according to the standard solar spectrum defined by the ASTM. The wavelength spectrum range of all ideal solar cells starts with the wavelength of 119 nm and ends at their bandgap wavelengths. Meanwhile, the spectrum partitioning of the real solar cells is based on the spectral external quantum given in their datasheets. The spectrum partitioning patterns of the ideal and real Si [5], GaAs [6], and Ge [7] solar cells for the different solar spectra are tabulated in Table 3-1 [j3].

Table 3-1 Spectrum Partitioning Pattern of the ideal/real Solar Cells.

Solar Cell	Ideal			Real		
	Si	GaAs	Ge	Si	GaAs	Ge
<b>Range [nm]</b>	119 – 1107	119 – 873	119 – 1850	350 – 1200	325 – 900	300 – 750
<b>Step [nm]</b>	38	29	66.58	34	23	58
<b>Number [#]</b>	27	27	27	26	26	26

### 3.2 Thermal-Electrical Model of Hybrid Photovoltaic-Thermoelectric Generator Systems

The study proposes a thermal-electrical model that describes the physical structure of two hybrid PV-TEG systems, stacked and parallel configurations, and identifies the parameters that affect the behavior of each configuration. In addition, it details the energy balance and the heat transfer mechanism within both configurations. Fig. 3.2 shows the schematic diagram of the stacked and parallel PV-TEG configurations

[j1]. Both configurations are composed of two main subsystems, the PV cell and the TEG subsystem.

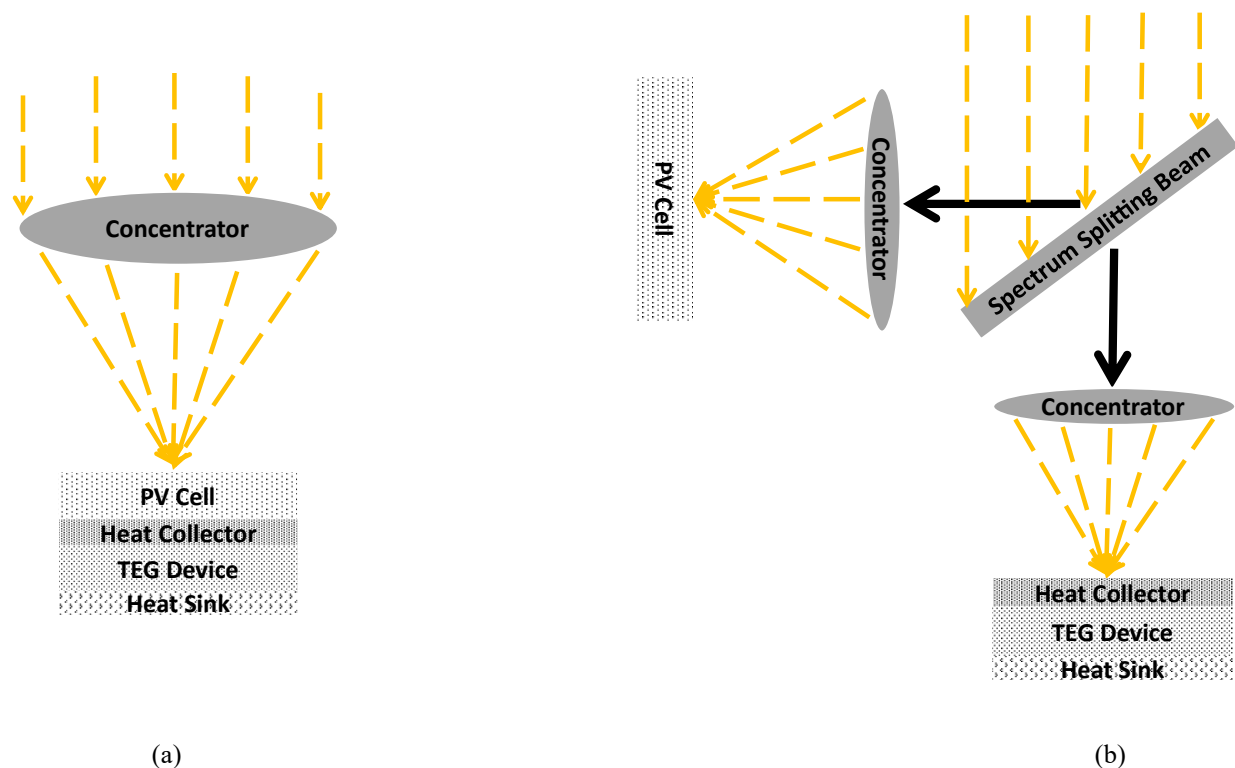


Fig. 3.2 The schematic diagram of a) the stacked and b) parallel hybrid PV-TEG system.

The PV cell is an mc-Si solar cell, and the TEG subsystem consists of a heat collector (HC), a TEG unit made from  $\text{Bi}_2\text{Te}_3$ , and a heat sink (HS). In the stacked configuration, the two subsystems are thermally coupled through the heat collector, which serves as a critical interface between the two subsystems, as seen in Fig. 3.2 (a). For the parallel configuration, the two subsystems are thermally decoupled, indicating an independent operation mechanism. A spectral beam splitter has been used to split the solar spectrum into two parts so that each device can operate efficiently, as seen in Fig. 3.2 (b). According to the energy of the incident photons, as the silicon PV cell bandgap is 1.12 eV, the within-bandgap spectrum of the range 300 nm – 1100 nm is transmitted to the PV cell, and the post-bandgap spectrum of the range 1100 nm – 4000 nm is transmitted to the TEG subsystem. This arrangement ensures that both devices operate at their optimal temperatures. The most common equation used to estimate the total input power based on their corresponding minimum ( $\lambda_{min, PV_{SA/ST/PL}/TEG_{PL}}$ ) and maximum ( $\lambda_{max, PV_{SA/ST/PL}/TEG_{PL}}$ ) spectral wavelength limits is given as follows [8]

$$P_{in, PV_{SA/ST/PL/TEG_{PL}}} = \eta_{opt} \times C_{g, PV/TEG} \times A_{PV/HC, PL} \times \int_{\lambda_{min, PV_{SA, ST, PL/TEG_{PL}}}^{\lambda_{max, PV_{SA, ST, PL/TEG_{PL}}}} F(\lambda)_{PV_{SA/ST/PL/TEG_{PL}}} d\lambda, \quad (3-1)$$

where  $F(\lambda)_{PV_{SA/ST/PL/TEG_{PL}}}$  is the solar spectral irradiance directed to the standalone PV cell, the PV cell in the stacked and parallel configurations, or the TEG subsystem in the parallel configuration,  $\eta_{opt}$  is the optical system efficiency of 0.95,  $A_{PV/HC, PL}$  is the surface area of the PV cell and the HC in the parallel configuration, and  $C_{g, PV/TEG}$  is the geometric concentration ratio of the PV cell or the TEG. In the stacked configuration, the geometric concentration ratio of the PV cell ( $C_{g, PV}$ ) is calculated as [9]

$$C_{g, PV} = A_{Con.} / A_{PV}. \quad (3-2)$$

While for the parallel configuration, for the same concentrator area ( $A_{Con.}$ ), the geometrical ratio of the TEG ( $C_{g, TEG}$ ) is coupled with that of the PV cell for equivalent energy harvesting of both devices, as follows

$$A_{Con.} = C_{g, PV} \times A_{PV} = C_{g, TEG} \times A_{HC, pl}. \quad (3-3)$$

Therefore, considering the designated surface areas of the PV cell and HC alongside a specified geometric concentration ratio of the PV cell, it becomes possible to ascertain the geometric concentration ratio for the TEG unit and evaluate the spectrum-based input power transferred to both devices. The input power of both configurations is calculated at the full spectrum of 300 nm- 4000 nm with a power density of 997.5 W/m<sup>2</sup>.

It should be noted that the front and back surface temperatures of the PV cell are assumed to be practically identical, as the PV cell is very thin; thus, a single temperature is considered for the PV cell. The temperature-dependent output power of the PV cell ( $P_{PV}$ ) at a specific light concentration level is evaluated as follows

$$P_{PV}(T_{PV}) = I_{SC}(T_{PV}) \times V_{OC}(T_{PV}) \times FF(T_{PV}), \quad (3-4)$$

where  $I_{SC}(T_{PV})$ ,  $V_{OC}(T_{PV})$  and  $FF(T_{PV})$  are the temperature-dependent short circuit current, open circuit voltage, and fill factor, respectively.

Fig. 3.3 represents the energy flow chart of the stacked configuration that has a thermal coupling between the PV cell with the TEG subsystem [c4]. A solar concentrator directs the full solar spectrum, ranging from 300 nm to 4000 nm, onto the PV cell at different concentration levels.

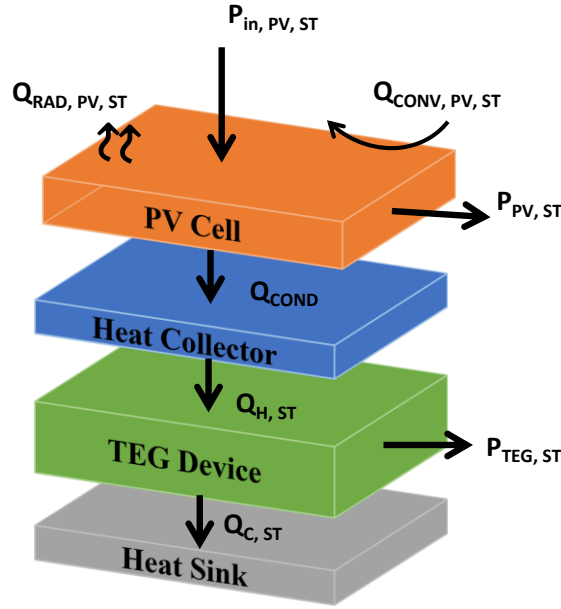


Fig. 3.3 Energy flow chart of the stacked PV-TEG system.

Following the energy flow of Fig. 3.3, the thermal balance equation describing the output power of the PV cell can be evaluated as follows [8]

$$P_{PV,ST}(T_{PV,ST}, T_{HC,ST}) = \alpha_{PV} \times P_{in,PV,ST} - Q_{RAD,PV,ST} - Q_{CONV,PV,ST} - Q_{COND}, \quad (3-5)$$

where  $T_{PV,ST}$  and  $T_{HC,ST}$  are the temperatures of the PV cell and the heat collector in the stacked configuration, respectively,  $\alpha_{PV}$  is the absorptivity of the PV cell,  $P_{in,PV,ST}$  is the input power transmitted to the PV cell in the stacked configuration of the full spectrum, ranging from 300 to 4000 nm, with a power density of  $997.5 \text{ W/m}^2$ ,  $Q_{COND}$  is the conducted heat, and  $Q_{RAD,PV,ST}$  and  $Q_{CONV,PV,ST}$  are the radiative and convective heat losses of the PV cell in the stacked configuration, respectively. Consequently, the absorbed heat at the TEG unit's hot side in the stacked configuration ( $Q_{H,ST}$ ) can be evaluated as the difference between the conduction heat and the released TEG unit's radiation losses, which can be described as follows [10]

$$Q_{H,ST}(T_{PV,ST}, T_{HC,ST}) = \alpha_{HC} \times Q_{COND}, \quad (3-6)$$

where  $\alpha_{HC}$  represents the absorptivity of the HC. It is further defined as the conducted heat from the heat collector to the TEG unit's hot side, determined by the difference of their respective temperatures, as follows [11]

$$Q_{H,ST}(T_{HC,ST}, T_{H,ST}) = (k_{HC} A_{HC,ST}/d_{HC})(T_{HC,ST} - T_{H,ST}), \quad (3-7)$$

where  $k_{HC}$ ,  $A_{HC,ST}$  and  $d_{HC} = 1$  mm are the thermal conductivity, surface area, and thickness of the HC, respectively, and  $T_{H,ST}$  is the temperature of the hot side of the TEG unit in the stacked configuration. The heat removed at the TEG unit's cold side in the stacked configuration ( $Q_{C,ST}$ ) can be represented as follows [11]

$$Q_{C,ST}(T_{C,ST}) = h_c \times A_{HS,ST} \times (T_{C,ST} - T_{Coolant}), \quad (3-8)$$

where  $T_{C,ST}$  and  $T_{Coolant}$  are the temperatures of the TEG unit's cold side in the stacked configuration and the coolant temperatures, respectively,  $h_c$  is the heat transfer coefficient of the HS, and  $A_{HS,ST}$  is the surface area of the HS in the stacked configuration, which is identical to the surface area of the HC.

Fig. 3.4 shows the schematic diagram of the parallel hybrid system where the two subsystems are thermally decoupled [c3]. A spectral beam splitter has been used to split the solar spectrum based on the energy of the incident photons. A solar concentrator directs the corresponding solar spectrum onto the PV cell and the TEG subsystems at different concentration levels.

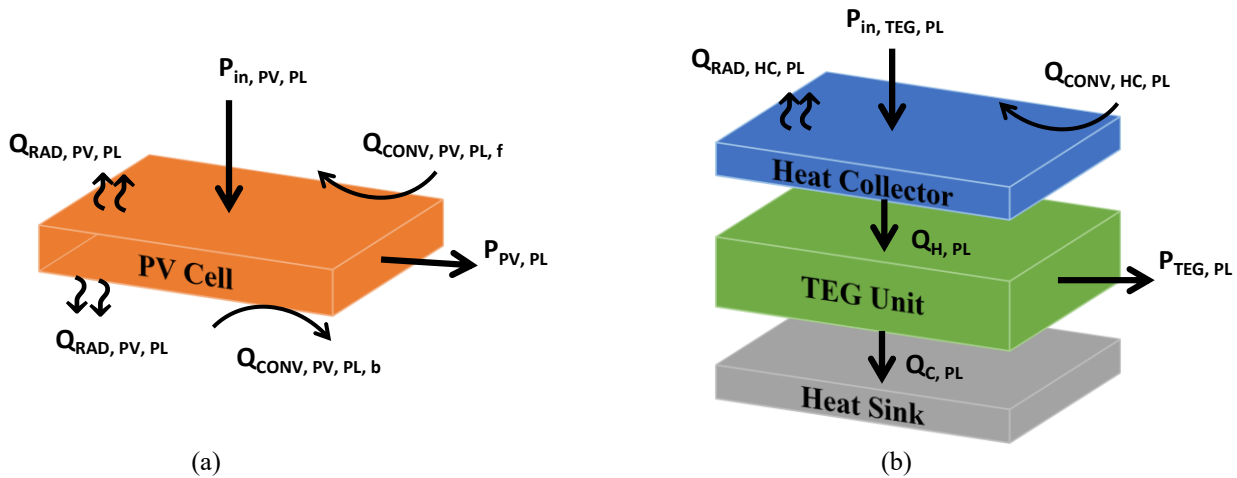


Fig. 3.4 Energy flow chart of the parallel PV-TEG system.

Following the energy flow of Fig. 3.4 (a), the output power of the PV cell in the parallel configuration ( $P_{PV,PL}$ ) can be characterized as follows [8]

$$P_{PV,PL}(T_{PV,PL}) = \alpha_{PV} \times P_{in,PV,PL} - Q_{RAD,PV,PL,f} - Q_{RAD,PV,PL,b} - Q_{CONV,PV,PL,f} - Q_{CONV,PV,PL,b}, \quad (3-9)$$

where  $T_{PV,PL}$  is the temperature of the PV cell in the parallel configuration,  $P_{in,PV,PL}$  is the input power transmitted to the PV cell in the parallel configuration of the full

spectrum, ranging from 300 to 1100 nm, with a power density of 802.2 W/m<sup>2</sup>, and  $Q_{RAD,PV,PL,f,b}$  and  $Q_{CONV,PV,PL,f,b}$  are the radiative and convective heat losses of the front and back surfaces of the PV cell in the parallel configuration, respectively. The HC has no thermal contact with the PV cell, so the sun is the heat energy source for the TEG subsystem. Following the energy flow of Fig. 3.4 (b), the heat absorbed at the hot side of the TEG unit in the parallel configuration ( $Q_{H,PL}$ ) is related to the spectrum-based input solar energy, HC's specification, and the radiation and convection heat losses of the TEG unit. This relationship can be described as follows [12]

$$Q_{H,PL}(T_{HC,PL}) = \alpha_{HC} \times P_{in,TEG,PL} - Q_{RAD,HC,PL} - Q_{CONV,HC,PL}, \quad (3-10)$$

where  $T_{HC,PL}$  is the temperature of the heat collector in the parallel configuration,  $P_{in,TEG,PL}$  is the input power transferred to the TEG unit of the bandgap spectrum, ranging from 1100 nm to 4000 nm, with a power density of 195.3 W/m<sup>2</sup>, and  $Q_{RAD,HC,PL}$  and  $Q_{CONV,HC,PL}$  are the radiative and convective heat losses of the heat collector in the parallel configuration, respectively. Similarly, the absorbed heat at the hot side of the TEG in the parallel configuration ( $Q_{H,PL}$ ) is evaluated as follows

$$Q_{H,PL}(T_{HC,PL}, T_{H,PL}) = (k_{HC} A_{HC,PL} / d_{HC})(T_{HC,PL} - T_{H,PL}), \quad (3-11)$$

where  $T_{H,PL}$  is the temperature of the TEG unit's hot side in the parallel configuration. The heat removed at the TEG unit's cold side in the parallel configuration ( $Q_{C,PL}$ ) can be represented as follows

$$Q_{C,PL}(T_{C,PL}) = h_c \times A_{HS,PL} (T_{C,PL} - T_{Coolant}), \quad (3-12)$$

where  $T_{C,PL}$  is the temperature of the TEG unit's cold side in the parallel configuration, and  $A_{HS,PL}$  is the surface area of HS in the parallel configuration, which is identical to the surface area of the HC. Two distinct thermal-electrical mathematical models are proposed. An iterative computational method to solve simultaneously the nonlinear equations of the proposed models is used, enabling precise prediction of overall system performance. The proposed mathematical model is programmed in MATLAB R2021a, in which the flow chart of the simulation process is summarized in Fig. 3.5 [j1].

The simulation in this chapter is carried out using an mc-Si solar cell [13] and the Bi<sub>2</sub>Te<sub>3</sub> TEG unit [14]. The surface area of the heat collector is identical to the surface area of the PV cell in the stacked configuration and is 250 mm<sup>2</sup> in the parallel

configuration. By simultaneously solving the set of equations of each system, the unknown parameters  $I_{SC}$ ,  $V_{OC}$ ,  $FF$ ,  $P_{PV}$ ,  $T_{PV}$ ,  $T_H$ ,  $T_C$ ,  $T_{HC}$ ,  $Q_H$ ,  $Q_C$  and  $I$  are evaluated.

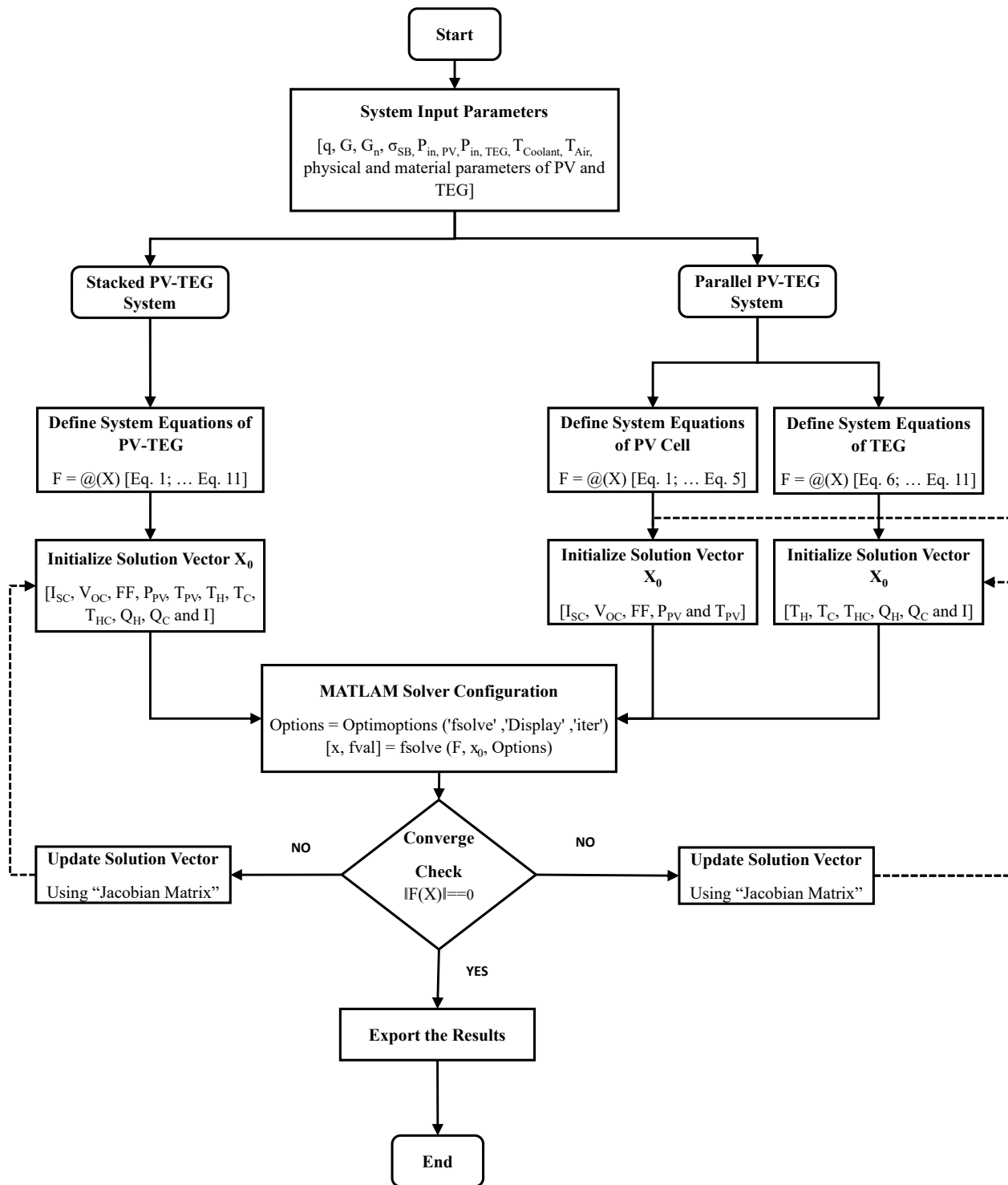


Fig. 3.5 The Simulation Process in MATLAB R2021a.

### 3.3 Key Parameter Investigation and Optimization of Hybrid PV-TEG Systems

The output performance of the PV-TEG hybrid systems varies by configuration. The stacked configuration does not prove superiority over the parallel configuration or even the standalone PV cell, although the parallel configuration offers a more effective solution through improved energy harvesting. The study investigates and carefully optimizes various key parameters, so the stacked configuration has the potential to become a promising solution, and the performance of the parallel configuration can be further improved. The key parameters include

- Temperature coefficient of the PV cell

The voltage temperature coefficient of the PV plays a vital role in determining its power temperature coefficient. The voltage temperature coefficient of the PV cell, as indicated in its datasheet, is  $-1.84 \text{ mV}/^\circ\text{C}$ . A 10 % lower value (less negative) of  $-1.656 \text{ mV}/^\circ\text{C}$  is used to evaluate the changes in the PV cell's temperature and PCE in each system.

- Geometric dimension of the TEG unit's legs

The performance of the TEG unit is related to the  $L_{n,p}$ , and  $A_{n,p}$  which in turn affects the overall efficiency of the Hybrid system. A  $\pm 10 \%$  change in length, width, and height of the TEG unit's n and p-legs are implemented as summarized in Table 3.3.

Table 3.3 Variation of the dimensions of the TEG unit's n and p-type legs.

Dimension of n and p-type Legs	Length		Area	
	Lower	Higher	Higher	Lower
Value	6.3	7.7	$11 \times 11$	$9 \times 9$

- Material characteristics of the TEG unit

The characteristics of the TEG unit's material, such as the Seebeck coefficient and electrical and thermal conductivity, determine its figure of merit, showing how efficient the TEG is. A 10 % increment of the Seebeck coefficient and electrical conductivity, and a 10 % decrement of the thermal conductivity are implemented as tabulated in Table 3.4. These enhancements improved the figure of merit of the TEG unit from 0.768 to 1.134. All key parameters are subsequently optimized for each configuration, and the simulation has been performed for 10%, 12.5% and 15% improvement in all the key parameters.

Table 3.4 The characteristics of the TEG's material with a 10 % enhancement.

Material Prosperities	Seebeck Coefficient		Electrical Conductivity		Thermal Conductivity	
	$S_p$ [ $\mu\text{V/K}$ ]	$S_n$ [ $\mu\text{V/K}$ ]	$\sigma_p$ [S/m]	$\sigma_n$ [S/m]	$K_p$ [W/m K]	$K_n$ [W/m K]
<b>Value</b>	224.07	-189.31	$8.3714 \times 10^4$	$9.8302 \times 10^4$	1.1385	0.9099

### 3.4 Spectrum Splitting-Based Hybrid PV-TEG Parallel Configuration

The study proposes a novel spectrum-splitting concept that identifies certain wavelength ranges within the within-bandgap spectrum which might be more effectively converted by the TEG subsystem than the PV cells. The proposed approach includes dividing the WBS between the PV cell and the TEG with a step of 50 nm while the post-bandgap spectrum is always transmitted to the TEG device. Therefore, fifteen different spectrum-splitting configurations were investigated. In the first configuration, the entire within-bandgap spectrum is transferred to the PV, and the post-bandgap spectrum is directed to the TEG. In the second configuration, the PBS and the spectrum range of 350- 400 nm are transferred to the TEG device, and the spectrum range of 400- 1100 nm is transmitted to the PV cell, and so on. Finally, in configuration 15, the post-bandgap spectrum and the spectrum range of 350 – 1050 nm are transmitted to the TEG device, and only the spectrum part of 1050 – 1100 is directed to the PV cell. Fig. 3.6 summarizes the 15 configurations of the proposed novel spectrum splitting concept [j2].

Spectrum Type	Spectrum Partition (nm)	Configuration																						
		1	2	3	4	5	6	7	8	9	10	11	12	13	14	15								
WBS	350 - 400	PV	TEG	PV	TEG	PV	TEG	PV	TEG	PV	TEG	PV	TEG	PV	TEG	PV	TEG							
	400 - 450		TEG		TEG		TEG		TEG		TEG		TEG		TEG		TEG	TEG	TEG	TEG	TEG	TEG	TEG	
	450 - 500		TEG		TEG		TEG		TEG		TEG		TEG		TEG		TEG	TEG	TEG	TEG	TEG	TEG	TEG	TEG
	500 - 550		TEG		TEG		TEG		TEG		TEG		TEG		TEG		TEG	TEG	TEG	TEG	TEG	TEG	TEG	TEG
	550 - 600		TEG		TEG		TEG		TEG		TEG		TEG		TEG		TEG	TEG	TEG	TEG	TEG	TEG	TEG	TEG
	600 - 650		TEG		TEG		TEG		TEG		TEG		TEG		TEG		TEG	TEG	TEG	TEG	TEG	TEG	TEG	TEG
	650 - 700		TEG		TEG		TEG		TEG		TEG		TEG		TEG		TEG	TEG	TEG	TEG	TEG	TEG	TEG	TEG
	700 - 750		TEG		TEG		TEG		TEG		TEG		TEG		TEG		TEG	TEG	TEG	TEG	TEG	TEG	TEG	TEG
	750 - 800		TEG		TEG		TEG		TEG		TEG		TEG		TEG		TEG	TEG	TEG	TEG	TEG	TEG	TEG	TEG
	800 - 850		TEG		TEG		TEG		TEG		TEG		TEG		TEG		TEG	TEG	TEG	TEG	TEG	TEG	TEG	TEG
	850 - 900		TEG		TEG		TEG		TEG		TEG		TEG		TEG		TEG	TEG	TEG	TEG	TEG	TEG	TEG	TEG
	900 - 950		TEG		TEG		TEG		TEG		TEG		TEG		TEG		TEG	TEG	TEG	TEG	TEG	TEG	TEG	TEG
	950 - 1000		TEG		TEG		TEG		TEG		TEG		TEG		TEG		TEG	TEG	TEG	TEG	TEG	TEG	TEG	TEG
	1000 - 1050		TEG		TEG		TEG		TEG		TEG		TEG		TEG		TEG	TEG	TEG	TEG	TEG	TEG	TEG	TEG
	1050 - 1100		TEG		TEG		TEG		TEG		TEG		TEG		TEG		TEG	TEG	TEG	TEG	TEG	TEG	TEG	TEG
PBS	1100 - 4000	TEG	TEG	TEG	TEG	TEG	TEG	TEG	TEG	TEG	TEG	TEG	TEG	TEG	TEG									

Fig. 3.6 Fifteen configurations of the proposed novel spectrum splitting concept.

The spectrum-based input power, which is transferred to the PV cell  $P_{in,PV}(\lambda_c)$  and the TEG device  $P_{in,TEG}(\lambda_c)$  can be evaluated as follows

$$P_{in,PV}(\lambda_c) = \eta_{opt} \times C_{g,PV} \times A_{PV} \times \int_{\lambda_c}^{1100} F(\lambda) d\lambda, \quad (3-13)$$

$$P_{in,TEG}(\lambda_c) = \eta_{opt} \times C_{g,TEG} \times A_{HC} \times \left\{ \int_{350}^{\lambda_c} F(\lambda) + \int_{1100}^{4000} F(\lambda) \right\} d\lambda, \quad (3-14)$$

where  $\lambda_c$  is the configuration-based cutoff wavelength. The minimum and maximum wavelength spectrum-wavelength limit corresponds to the spectrum-splitting pattern shown in Fig. 3.6.

The Thermal-electrical mathematical model is proposed in chapters 1 and 3. For each configuration, by simultaneously solving the set of equations of the parallel configuration, the unknown parameters  $I_{SC}|_{\lambda_c}^{1100}$ ,  $V_{OC}|_{\lambda_c}^{1100}$ ,  $FF|_{\lambda_c}^{1100}$ ,  $P_{PV}|_{\lambda_c}^{1100}$ ,  $T_{PV}|_{\lambda_c}^{1100}$ ,  $T_H|_{350}^{\lambda_c}|_{1100}^{4000}$ ,  $T_C|_{350}^{\lambda_c}|_{1100}^{4000}$ ,  $T_{HC}|_{350}^{\lambda_c}|_{1100}^{4000}$ ,  $Q_H|_{350}^{\lambda_c}|_{1100}^{4000}$ ,  $Q_C|_{350}^{\lambda_c}|_{1100}^{4000}$  and  $I|_{350}^{\lambda_c}|_{1100}^{4000}$  can be evaluated.

The output power of the TEG unit can be evaluated as follows [15]

$$P_{TEG}|_{350}^{\lambda_c}|_{1100}^{4000} = Q_H|_{350}^{\lambda_c}|_{1100}^{4000} - Q_C|_{350}^{\lambda_c}|_{1100}^{4000}. \quad (3-15)$$

The overall output power of the parallel configuration  $P_{PV-TEG}|_{350}^{4000}$  for each configuration can be evaluated as follows

$$P_{PV-TEG}|_{350}^{4000} = P_{TEG}|_{350}^{\lambda_c}|_{1100}^{4000} + P_{PV}|_{\lambda_c}^{1100 \text{ nm}}. \quad (3-16)$$

The overall efficiency  $\eta_{PV-TEG}|_{350}^{4000}$  of the hybrid system can be evaluated at each configuration as

$$\eta_{PV-TEG}|_{350}^{4000} = \frac{P_{TEG}|_{350}^{\lambda_c}|_{1100}^{4000} + P_{PV}|_{\lambda_c}^{1100 \text{ nm}}}{P_{in}|_{350}^{4000 \text{ nm}}}. \quad (3-17)$$

## 4 New Scientific Results

### 4.1 Thesis group 1: Extending the SDM of Solar Cells Under Different Solar Spectra

The simulation is carried out for ideal and real Si, GaAs, and Ge solar cells at a temperature of 25 °C, and a power density of 1000 W/m<sup>2</sup>. The ideal solar cells have the same surface area as 1 cm<sup>2</sup>.

#### Wavelength-based Efficiency

Fig. 4.1 (a) illustrates the wavelength-based efficiency of the ideal Si, GaAs, and Ge solar cells. The wavelength-based efficiency of all solar cells increases linearly at different slopes with the wavelength increase. The increase in efficiency with the wavelength reflects the increasing number of photons available for absorption as the wavelength approaches the bandgap, where the maximum efficiency is obtained at the bandgap wavelength. The sharp drop in efficiency beyond the bandgap wavelengths corresponds to their inability to absorb lower-energy photons. This provides valuable insights into each material's spectral sensitivity. GaAs solar cell demonstrates a steeper rise in efficiency in the visible spectrum due to its optimal and direct bandgap nature, which allows it to absorb and convert visible light more efficiently compared to Si and Ge cells.

Fig. 4.1 (b) shows the wavelength-based efficiency of Si, GaAs, and Ge solar cells at realistic operating conditions, which peak at a wavelength below the bandgap, and then decreases toward zero near the bandgap. This is attributed to the practical limitations of real solar cells, such as recombination, non-radiative losses, and inefficient absorption. Only photons with energy equal to or just above the bandgap contribute efficiently to electron-hole pair generation, while photons with much higher energy led to thermal losses, and those with lower energy are not absorbed. The GaAs cell exhibits a maximum efficiency within the visible spectrum of 800 - 870 nm, making it preferable for space or satellite systems, concentrated systems, and specialized terrestrial uses. The Si cell peaks slightly later around 950 - 1100 nm with a lower peak efficiency due to its indirect bandgap and keeps a moderate efficiency across a broader spectrum range, making it the dominant technology for residential, commercial, and terrestrial installations. As the Ge exhibits the broadest response it can be used in multi-junction solar cells where Ge is often used as a bottom cell and is advantageous for certain applications, such as infrared and low-light applications.

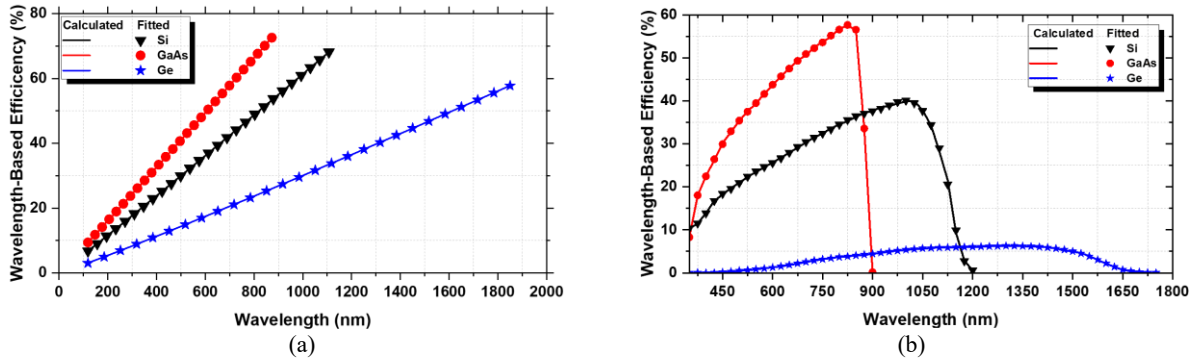


Fig. 4.1 Wavelength-based efficiency of a) ideal and b) real Si, GaAs, and Ge real cells.

**Wavelength-dependent real Output Power**

The real wavelength-dependent output power of the ideal and real solar cells under AM0 and AM1.5 G solar spectra can be calculated based on a straightforward procedure. This involves the multiplication of wavelength-based efficiency (as depicted in Fig. 4.1) by the solar spectra. The calculations are tailored to the specific bandgap of each solar cell. Fig. 4.2 shows the real wavelength-dependent output power of the ideal and real solar cells for different solar spectra. The performance gap between AM0 and AM1.5G conditions is most pronounced for Si cells. This underscores the importance of spectral considerations in predicting the real-world performance of terrestrial solar installations. The GaAs cell demonstrates the highest output power through its operating wavelength range, indicating its superior performance in the visible spectrum. The Si cell exhibits a lower peak output power through the visible to near-infrared wavelength spectrum, featuring a broader spectral response compared to the GaAs solar cell. While the Ge cell offers the broadest spectrum response extending to the far infrared spectrum, it demonstrates the lowest output power among the three solar cells.

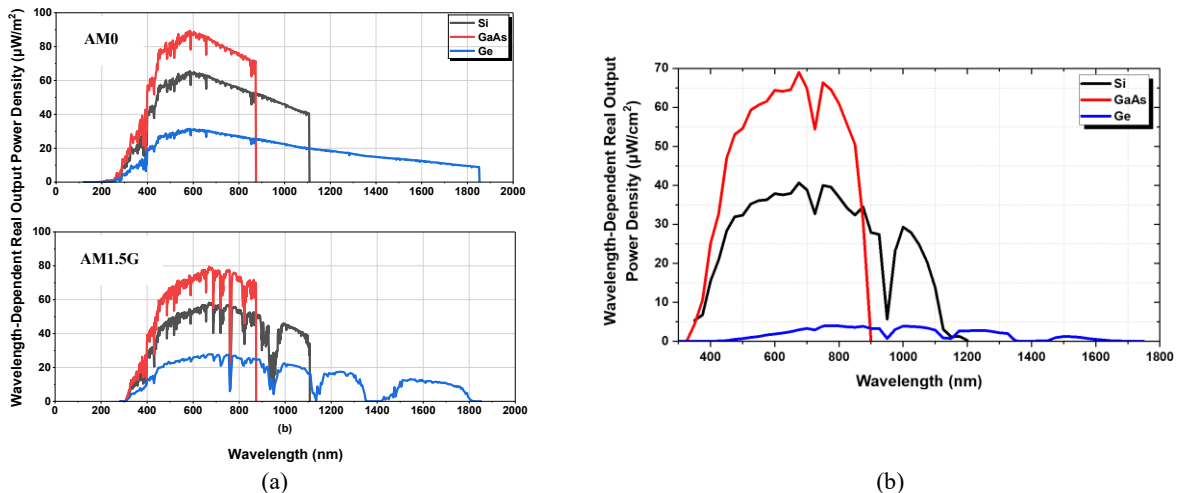


Fig. 4.2 Real wavelength-dependent output power of the a) ideal and b) real Si, GaAs, and Ge solar cells different solar spectra

## Concept Validation

The integration of the wavelength-dependent real output power functions of each ideal and real solar cell along its corresponding wavelength spectrum range results in the average output power under the different solar spectra. The average output power of the ideal Si, GaAs, and Ge solar cells under AM0 and AM1.5G solar spectra is (40 mW and 32.9 mW), (39 mW and 32.7 mW), and (29 mW and 22 mW), respectively. On the other hand, the average output power of the real Si, GaAs, and Ge solar cells under the AM1.5G solar spectrum is 3.4285 W, 27.3 mW, and 66.585  $\mu$ W, respectively. Then the power conversion efficiency of the ideal and real solar cells under the different solar spectra is evaluated and compared to the Shockley–Queisser limit and their respective datasheet values as seen in Table 4.1.

Table 4.1 SQ Limit and Datasheet Validation of the Ideal and Real Solar Cells, respectively.

Solar cell	Ideal				Real	
	AM0		AM1.5G		AM1.5G	
	Calculated (%)	SQ Limit (%)	Calculated (%)	SQ Limit (%)	Calculated (%)	Datasheet (%)
Si	29.644	29.990	32.963	33.050	22.41	22.55
GaAs	29.500	29.850	32.741	32.920	27.57	27.60
Ge	21.859	21.910	22.557	22.668	2.460	2.630

My contributions are summarized as follows

**Thesis 1** I have extended the single diode model (SDM) of the solar cell by incorporating spectral sensitivity into the photogenerated current. I have implemented this model for three solar cells characterized by different bandgap energies, including silicon (Si), gallium arsenide (GaAs), and germanium (Ge) solar cells, at both ideal and realistic operating conditions. The model is capable of handling changes in the input spectrum and adjusting power output of the modelled solar cells, accordingly, showing different output characteristics, even though their theoretical limits are nearly identical. In addition, the model is capable of determining the wavelength-based efficiency and wavelength-dependent real power output of each solar cell at both ideal and realistic operating conditions across different solar spectra. Furthermore, the model reproduces both the Shockley-Queisser limit in the case of ideal solar cells and the correct nominal efficiency value and power rating for real solar cells with sufficient accuracy (below 1.5 % and below 2.5 % MAPE, respectively).

**Related Publications:** The thesis's main concept has been published in [j1] and [C5].

## 4.2 Thesis group 2: Thermal-Electrical Model of Photovoltaic-Thermoelectric Generator Systems

### Standalone PV Cell

Fig. 4.3 (a) depicts the output power of the standalone PV cell across different light concentration levels. A portion of the input solar power transferred to the PV cell is inevitably lost due to optical losses ( $Q_{Opt,PV}$ ), which is 10 % of  $P_{in,PV,SA}$  according to the value of the PV cell's absorptivity. These optical losses increase proportionally with the concentration ratio, reducing the effective input power available for conversion. However, the input solar power transferred to the standalone PV cell is partially able to offset the increasing losses. Consequently, this sustains increasing output power of the standalone PV cell with the increase in the light intensity. Due to elevated temperatures, the rate of increase of the output power is already impeded, and the fraction of thermal losses is increased, leading to a decrease in electric efficiency. Fig. 4.3 (b) illustrates that the PV efficiency diminishes with the increase of the light intensity. Therefore, operating the PV cell in such operational conditions suppresses the advantage of light concentration, indicating how the PV cell's temperature coefficient parameters are important.

### PV Cell - Stacked Vs. Parallel Configurations

Fig 4.4 (a) depicts that the output power of the PV cell in both configurations increases with the increase of the light concentration level. This is mainly a result of the increase in current (see dissertation), however, it is somewhat counteracted by the decrease in both the  $V_{OC}$  and  $FF$  of the PV cell. At each light concentration level, while the PV cell in the stacked configuration receives higher solar power input, its output power is lower as it exhibits higher temperature and thermal losses. This has a detrimental impact on the output power despite the increase of  $I_{SC}$ , particularly noticeable at higher light concentration levels. Fig. 4.4 (b) shows the PCE of the PV cell in both configurations, which decreases with the increase of the light concentration level. That is, the PV cell's high temperature in both configurations negatively affects its power output. Moreover, at each concentration level, the efficiency of the PV cell in the parallel configuration is higher than that in the stacked configuration. By comparing Fig. 4.3 (b) and Fig. 4.4 (b), the PCE of the PV cell in the stacked configuration is lower than in the case of the standalone PV cell due to the thermal resistance of the thermally coupled TEG. On the other hand, splitting the spectrum in a parallel configuration overcomes even the negative effects of the high temperature of the standalone PV cell, since input power is decreased in comparison to the standalone PV cell.

### **TEG Subsystem - Stacked Vs. Parallel Configurations**

The ratio of the removed-to-absorbed heat of the TEG unit ( $Q_C/Q_H$ ) serves as an indicator of how different configurations affect its performance. The ratio of the TEG unit in the stacked and parallel configurations decreases to 92.6 % and 91.4 % demonstrating that the output power of the TEG unit in both configurations increases with the increase of light concentration levels as seen in Fig. 4.5 (a). Accordingly, the TEG efficiency is up to 7.3 % and 8.5 % at  $C_{g,PV} = 5$  and  $C_{g,TEG} = 306$ , respectively, as seen in Fig. 4.5 (b). However, relative to the total input power density of  $997.5 \text{ W/m}^2$ , its contribution to the overall efficiencies of the stacked and parallel configurations reaches up to 0.9044 % and 1.399 % at  $C_{g,PV} = 5$  and  $C_{g,TEG} = 306$ , respectively. In addition, at each concentration ratio, the TEG unit in the stacked configuration exhibits a higher  $Q_C/Q_H$  ratio than that in the parallel configuration, resulting in a lower output power, as seen in Fig. 4.5 (a). This is attributed to the stacked configuration, where a larger HS enhances the heat extraction on the cold side relative to the heat absorption on its hot side. Accordingly, at each concentration level, the ECE of the TEG unit in the parallel configuration exceeds that in the stacked configuration, as seen in Fig. 4.5 (b).

### **Hybrid PV-TEG system - Stacked Vs. Parallel Configurations**

Fig. 4.4 (a) shows that the high junction temperature in the stacked configuration decreases the output power of the PV cell, even compared to the standalone PV cell. Meanwhile, Fig 4.5 (a) indicates that the TEG unit fails to compensate for the decrease in the PV's cell output power, primarily due to the low conducted input power to the TEG unit. On the other hand, splitting the spectrum in the parallel configuration enables the PV cell to operate at a lower temperature, resulting in a slightly higher output power of the PV cell than that in the stacked configuration, and gets more significant at a higher light concentration level. At the same time, the TEG unit has much more transferred input power than that in the stacked configuration, which results in much higher output power, especially at higher light concentration levels. This leads to a higher overall output power of the parallel configuration than the stacked configuration, and it gets more significant at higher light concentration levels, as seen in Fig. 4.6 (a). At each concentration ratio, the parallel configuration has higher overall efficiency than the stacked configuration and becomes more significant at higher concentration levels, as seen in Fig. 4.6 (b). In addition, it demonstrates that the overall efficiency of the stacked configuration is less than the standalone PV cell. While the parallel configuration has an advantage over the standalone PV cell. The overall output power and efficiency of both configurations at the different light concentration levels are tabulated in Table 4.3.

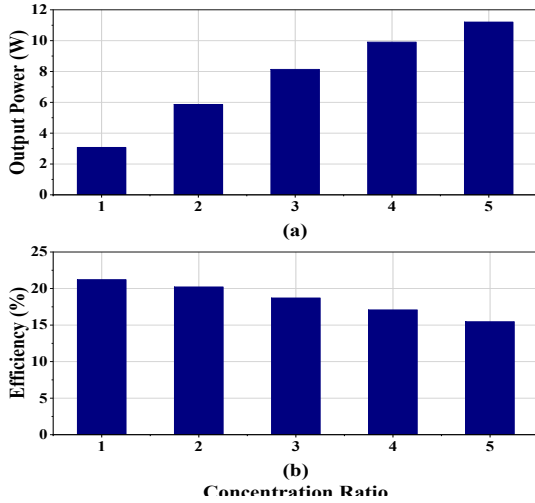


Fig. 4.3 a) Output power and b) PCE of the standalone PV cell for different light concentration levels.

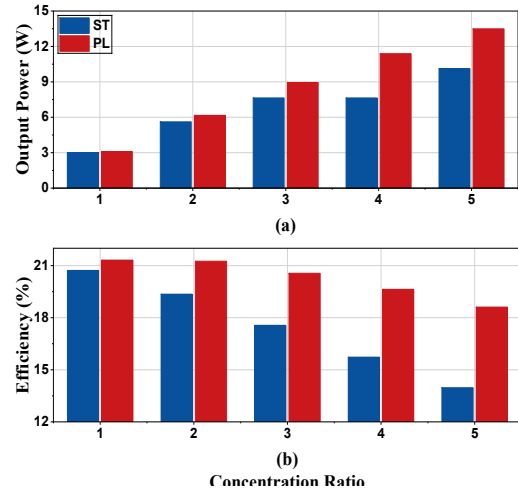


Fig. 4.4 a) Output power and b) PCE of the PV cell in both configurations for different light concentration levels.

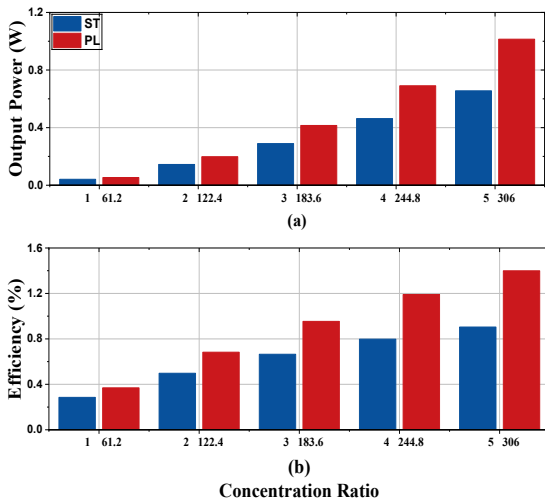


Fig. 4.5 a) Output power and b) ECE of the TEG unit in both configurations for different light concentration levels.

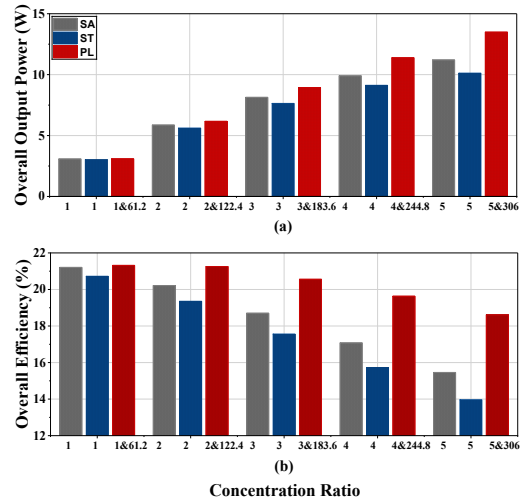


Fig. 4.6 Overall, a) output power and b) efficiency of the standalone PV cell and stacked and parallel configurations.

Table 4.3 The overall efficiency of the stacked and parallel hybrid systems.

Output Power [W]	$C_{g,PV}$				
	1	2	3	4	5
$P_{PV,SA}$	3.0747	5.8609	8.1330	9.9020	11.205
$P_{PV-TEG,ST}$	3.0042	5.6116	7.6371	9.120	10.121
$P_{PV-TEG,PL}$	3.0905	6.1622	8.9408	11.384	13.489
Efficiency [%]	$C_{g,PV}$ & $C_{g,TEG}$				
	1 & 61.2	2 & 122.4	3 & 183.6	4 & 244.8	5 & 306
$\eta_{PV,SA}$	21.207	20.212	18.699	17.074	15.456
$\eta_{PV-TEG,ST}$	20.720	19.352	17.558	15.725	13.962
$\eta_{PV-TEG,PL}$	21.315	21.251	20.555	19.630	18.607

My contributions are summarized as follows

**Thesis 2** I have developed an accurate and reliable thermal-electrical mathematical modeling framework applicable for stacked and parallel hybrid PV-TEG configurations to address the fundamental performance limitations of standalone PV cells operating without active cooling mechanisms.

- 2.1** I have proved that the thermal resistance introduced by the stacked configuration forces most of the heat to dissipate through the PV cell and reduces heat conducted to the TEG unit (approx. 15 % of the input power). However, spectrum-splitting reduces the PV cell temperature by 60 K at  $C_{g,PV} = 5$  and enables a higher heat transferred to the TEG unit up to 19.6%.
- 2.2** I have demonstrated that at  $C_{g,PV} = 5$  &  $C_{g,TEG} = 306$ , the overall efficiency of the parallel configuration is 20.4% higher than the standalone PV cell efficiency and 33.3% higher than the stacked configuration efficiency.
- 2.3** I have found that the efficiency improvement of the parallel configuration with current TEG technologies is more attributed to the temperature decrease of the PV cell (92.5% of the yield) than the power generated by the TEG (7.5% of the yield).

**Related Publications:** The thesis's main concept has been published in [j2]. Some modeling concepts of the presented model have been published in [C1], [C3], and [C4].

### 4.3 Thesis 3: Key Parameters Investigation and Optimization of the Hybrid PV-TEG Systems

#### Voltage Temperature Coefficient

Fig. 4.7 illustrates that at 10 % lower voltage temperature coefficient; the overall efficiency of both configurations increases with the increase of concentration levels. A lower voltage temperature coefficient results in a slightly reduced temperature of the PV cell in both configurations. The effect is subtle at lower concentrations and becomes more notable at higher concentration levels. Consequently, an improved PCE of the PV cell in both configurations is obtained compared to the standard case (at nominal parameters) and becomes more notable at higher concentration levels. At each concentration level, the decrease in the PV cell’s temperature is more pronounced in the stacked configuration than in the parallel configuration. As a result, the increase in the PCE of the PV cell in the stacked configuration is higher.

On the other hand, thermal coupling between the PV cell and the TEG unit in the stacked configuration leads to a change in the performance of the TEG unit. At a lower voltage temperature coefficient value, the ECE of the TEG in the stacked configuration decreases due to the decrease in the junction point temperature. However, this decrease is relatively small compared to the increase in the PCE of the PV cell, e.g., the ECE of the TEG unit only decreases by 0.024 % against an increase of 1.5 % in the PV cell efficiency at  $C_{g,PV} = 5$ .

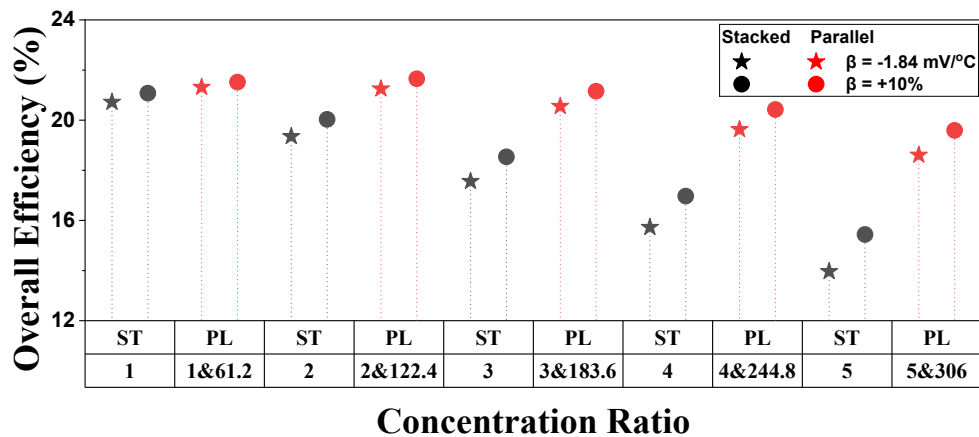


Fig. 4.7 The overall efficiency of both configurations for different voltage temperature coefficients.

**Geometric Dimension of TEG Legs**

In the parallel configuration, longer legs contribute to raising the temperature of the hot side, which increases the ECE of the TEG unit, and gets more significant at higher concentration levels. In contrast, shorter legs reduce the thermal resistance that allows for more heat to flow, resulting in lower temperature gradient and efficiency. The case is different in the stacked configuration, in that the longer legs increase the PV cell’s temperature and thus decrease the PV cell’s PCE. In addition, this leads to higher  $Q_{Losses,PV}$ , which reduces the power conducted to the TEG unit, resulting in a decrease in efficiency. Consequently, decreasing the length of the TEG’s legs in the stacked configuration limits these constraints, resulting in higher ECE of the TEG. (See dissertation)

On the other hand, in the stacked configuration, the TEG acts as a heat sink for the PV cell, where a larger surface area of the TEG legs enhances its ability for heat extraction, reducing the PV cell temperature and then increasing its efficiency. At the same time, this interprets the increase in ECE of the TEG unit, where the hot side has a higher temperature. In the parallel configuration, larger surface areas increase the thermal conductance, which means more heat flows through the device. This results in a lower temperature gradient and consequently decreases the ECE of the TEG unit, which becomes notable at higher concentration levels. (See dissertation)

Fig. 4.8 depicts the overall efficiencies of both configurations with TEG legs’ dimensions of  $6.3 \times 11 \times 11 \text{ mm}^3$  and  $7.7 \times 9 \times 9 \text{ mm}^3$ . It shows that both configurations have higher overall efficiency compared to the standard case, with a more pronounced enhancement observed for the stacked configuration.

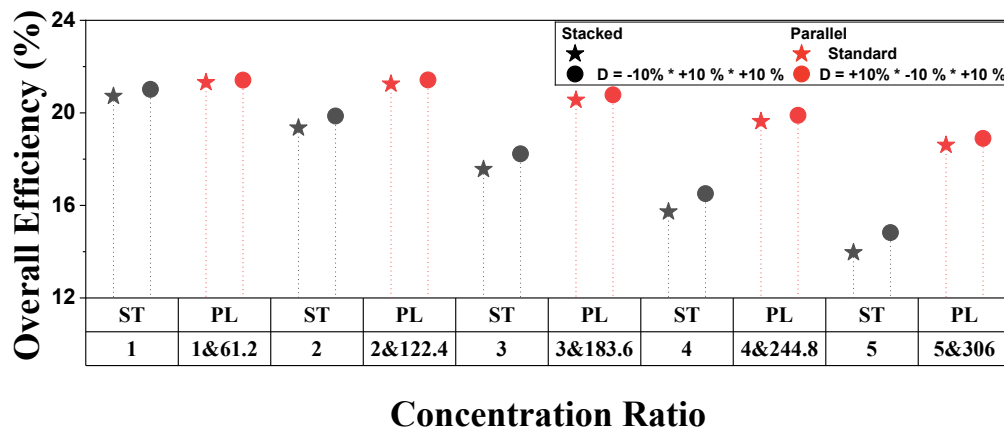


Fig. 4.8 The overall efficiency of both configurations for different lengths and areas of the n and p-type legs of the TEG unit.

**Material Properties of TEG Unit**

In the stacked configuration, as compared to the standard case, increasing the Seebeck coefficient increases the rate at which the TEG can absorb heat from the PV cell. Moreover, enhances the Peltier effect at the cold side, which helps in removing more heat from the PV-TEG junction, leading to an increase in the PCE of the PV cell. In addition, increasing the electrical conductivity of the TEG’s material decreases the Joule heat losses. This results in a more efficient conversion of the thermal heat, which contributes to removing more heat from the PV cell, leading to an increase in the PV cell’s efficiency. Ultimately, decreasing thermal conductivity impedes the heat flow through the TEG unit due to the increased thermal resistance. This increases the PV cell temperature and decreases its efficiency. (See dissertation)

On the other hand, an improved Seebeck coefficient or electrical conductivity or a reduced thermal conductivity increases the ECE of the TEG unit in both configurations. In the stacked configuration, the Seebeck effect exerts the strongest effect on the ECE of the TEG among the other characteristics, followed by the electrical conductivity. However, in the parallel configuration, the thermal conductivity has the highest influence, followed by the Seebeck coefficient (See the dissertation). As a result, a higher Seebeck coefficient or electrical conductivity increases the overall efficiency of the stacked configuration, while reduced thermal conductivity makes it lower. However, the parallel configuration delivers higher overall efficiency for the reduced thermal conductivity. (See dissertation)

Fig. 4.9 shows that the overall efficiency of each configuration increases for the improved material properties, showing

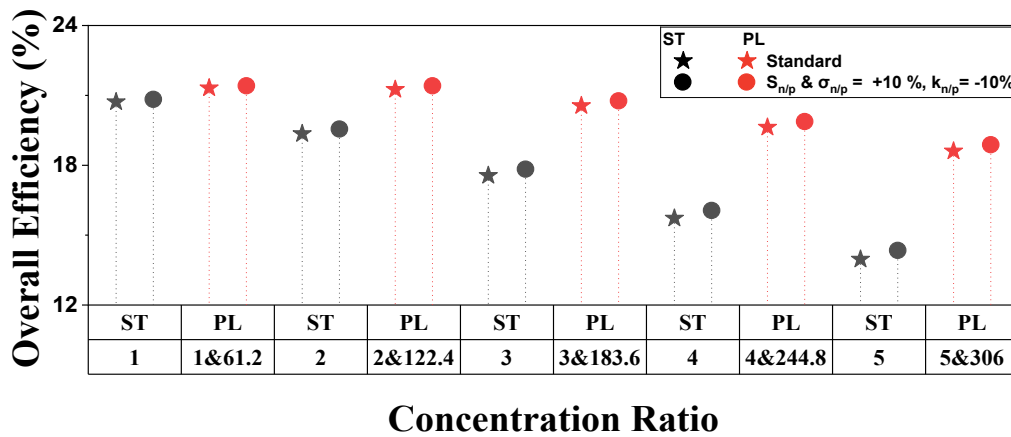


Fig. 4.9 The overall efficiency of both configurations for the different material characteristics of the TEG unit.

Table 4-4 tabulates the overall efficiency of each configuration at 10% improvements in voltage temperature coefficient of the PV cell, geometric dimensions of the TEG legs or their material properties.

Table 4-4 The overall efficiency for the different optimized key parameters of both configurations.

Stacked configuration	$C_{g,PV}$				
	1	2	3	4	5
$\beta = +10\%$	21.074	20.032	18.535	16.969	15.439
$D_{n,p} = (-10\%) \times (+10\%) \times (+10\%)$	21.018	19.866	18.230	16.509	14.823
$S_{n,p} = +10\%$ , $\sigma_{n,p} = +10\%$ and $k_{n,p} = -10\%$	20.832	19.554	17.834	16.062	14.348
Parallel configuration	$C_{g,PV} \ \& \ C_{g,TEG}$				
	1 & 61.20	2 & 122.4	3 & 183.6	4 & 244.8	5 & 306.0
$\beta = +10\%$	21.518	21.653	21.156	20.426	19.591
$D_{n,p} = (+10\%) \times (-10\%) \times (-10\%)$	21.417	21.425	20.781	19.893	18.897
$S_{n,p} = +10\%$ , $\sigma_{n,p} = +10\%$ and $k_{n,p} = -10\%$	21.410	21.412	20.765	19.876	18.881

### Key Parameters Optimization

The simulation was carried out for 12.5 % and 15 % enhancement of the key parameters, and the results are compared to the case of 10 % enhancement and the standard case.

The increase in the PCE of the PV cell in the stacked configuration relative to the standard case is greater than that in the parallel configuration. This is because the low voltage temperature coefficient of the PV cell offers a greater advantage for the stacked configuration. For example, at  $C_{g,PV} = 5$  and 15 % enhancement, the PCE of the PV cell in the stacked configuration increased by 37.3% while it is just 8.5 % rise in the case of the parallel configuration, relative to the standard case. (*See dissertation*)

On the other hand, the increase in ECE of the TEG unit is more pronounced in the parallel configuration than in the stacked configuration, due to the advantage of thermal decoupling. For example, at  $C_{g,PV} = 5$  and  $C_{g,TEG} = 306$ , and 15 % enhancement, the ECE of the TEG unit in the stacked and parallel configurations increased by 40 % and 66.7 %, respectively, compared to the standard case. Therefore, the thermal coupling between the PV cell and TEG unit in such stacked configurations makes adjusting these parameters crucial. (*See dissertation*)

As a result, Fig. 4.10 shows that the overall efficiency of the stacked configuration at  $C_{g,PV} = 1$  is higher than that of the parallel configuration. Otherwise, the parallel configuration is higher. In addition, the increase in the overall efficiency of the stacked configuration is higher than that of the parallel efficiency, compared to the standard case. This demonstrates that the PV cell contributes more significantly to the overall efficiency than the TEG unit for the optimized parameters. Moreover, the optimized key parameters have improved the stacked configuration to be a promising solution compared to the standalone PV cell.

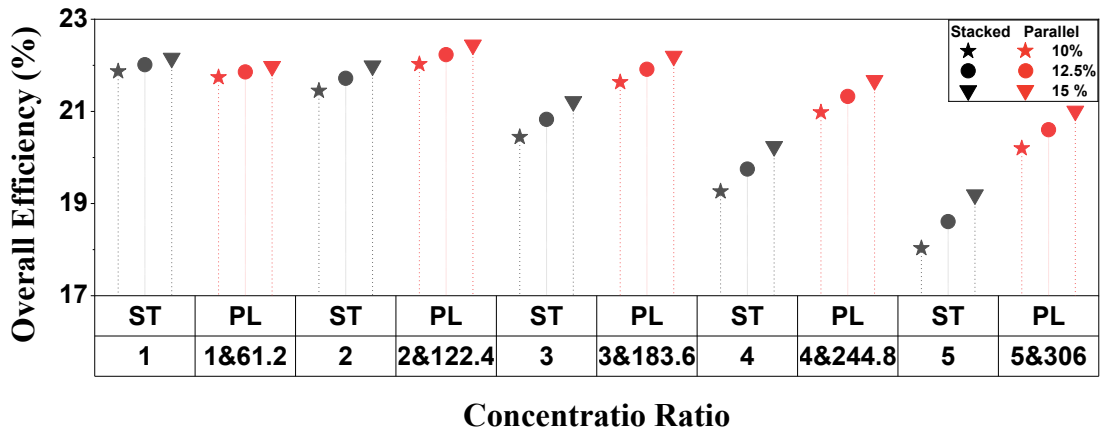


Fig. 4.10 The overall efficiency of both configurations for the 10%, 12.5%, and 15% enhancements.

Table 4-5 tabulates the overall efficiency of each configuration at 10%, 12.5% and 15% improvements of voltage temperature coefficient of the PV cell, geometric dimensions of the TEG legs and their material properties.

Table 4-5 The overall efficiency for the 10 %, 12.5 % and 15 % optimization of both configurations.

Stacked configuration	$C_{g,PV}$				
	1	2	3	4	5
Standard	20.720	19.352	17.558	15.725	13.962
10%	21.869	21.448	20.443	19.262	18.030
12.5 %	22.012	21.718	20.827	19.748	18.607
15%	22.157	21.990	21.214	20.239	19.191
Parallel configuration	$C_{g,PV}$ & $C_{g,TEG}$				
	1 & 61.20	2 & 122.4	3 & 183.6	4 & 244.8	5 & 306
Standard	21.315	21.251	20.555	19.630	18.607
10%	21.740	22.024	21.633	20.978	20.199
12.5 %	21.856	22.231	21.914	21.324	20.602
15%	21.978	22.442	22.199	21.673	21.007

My contributions are summarized as follows

**Thesis 3** I have conducted a comprehensive performance investigation and multi-parameter optimization of stacked and parallel PV-TEG configurations for different key parameters, including the temperature coefficient of the PV cell (voltage temperature coefficient), geometric dimensions of the TEG legs (width, height, and length), and their material properties (Seebeck coefficient, thermal and electrical conductivities).

**3.1** I have shown that at  $C_{g,PV} = 5$  &  $C_{g,TEG} = 306$ , a 10% improvement in the PV voltage temperature coefficient, TEG leg geometry, and TEG material properties increases the overall efficiency of the stacked configuration by 10.6%, 6.2%, and 2.8%, and of the parallel configuration by 5.3%, 1.6%, and 1.5%, respectively.

**3.2** I have proved that at  $C_{g,PV} = 5$  &  $C_{g,TEG} = 306$  with 15% multi parameter-optimization, the enhancement in PV cell efficiency is greater in the stacked configuration (37.3% vs. 8.5%), whereas the TEG efficiency improvement is more pronounced in the parallel configuration (66.7% vs. 40%).

**3.3** I have demonstrated that a shorter leg, larger surface area and higher thermal conductivity are ideal for the stacked configuration, whereas the opposite trends apply to the parallel configuration. Additionally, TEG efficiency benefits most from Seebeck coefficient in the stacked configuration and from thermal conductivity in the parallel configuration.

**Related Publications:** The thesis's main concept has been published in [j2]. Some optimization concepts of the presented model have been published in [C2].

## 4.4 Thesis 4: Spectrum Splitting-Based Hybrid PV-TEG Parallel Configuration

### Two-Split spectrum Hybrid Parallel Configuration

As a reference, the performance of a standalone PV cell has been evaluated at different light concentration levels. It has been compared with the performance of the hybrid system, where the entire within-bandgap spectrum of the range 350 nm – 1100 nm is transferred to the PV cell, while the post-bandgap spectrum of the 1100 nm- 4000 nm range is directed to the TEG device. Fig. 4.12 shows the efficiency of the full spectrum illuminated standalone PV cell versus the efficiency of the hybrid system at different light concentration levels. At a light concentration level of 5 suns, the PV cell efficiency decreases to about 16.565 % and the hybrid system's efficiency is 19.187 %.

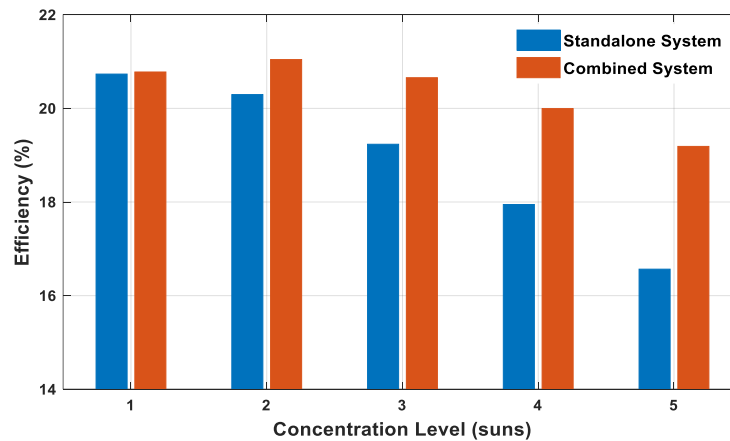


Fig. 4.12 Efficiency of a standalone PV cell against the hybrid system of the two-split spectrum.

### Proposed Spectrum Splitting

As a next step, the possibility of splitting the within-bandgap spectrum was investigated, with the configurations shown in Fig. 3.6. Geometrical concentration ratios of 1 and 51 suns are used for the PV cell and TEG device, respectively. The PV cell temperature decreases as the spectrum range transferred to the PV device is narrowed. Also, the solar cell efficiency decreases due to the decrease in the PV cell input power density as the spectrum partition ranges get smaller.

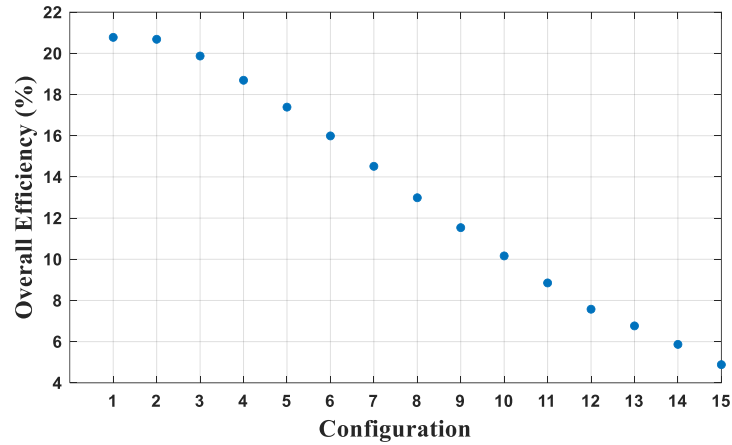
The maximum PV efficiency is 20.569 % at the spectrum partition of 350 – 1100 nm. With the increasing number of spectrum partitions (and thus the power density) directed to the TEG, the temperature difference between the TEG sides rises, which in turn increases the TEG efficiency. Fig. 4.13 shows the overall efficiency of the hybrid PV-TEG system of the fifteen configurations. Overall efficiency decreases as

the configuration goes from 1 to 15, e. g. more and more spectral components are directed to the TEG. The maximum overall efficiency is about 20.777 % at configuration 1, where the spectrum partitions of 350 – 1100 nm and 1100 – 4000 nm are transmitted to the PV cell and TEG device, respectively. The calculations of the hybrid PV-TEG system according to the spectrum-splitting pattern are tabulated in the dissertation. It can be clearly seen that the decrease in solar cell efficiency is higher than the increase in TEG efficiency, thus reducing overall system efficiency. Therefore, even though the solar cell temperature decreases, it cannot compensate for the low PCE that is characteristic of TEG devices. However, splitting the spectrum could counteract the negative effect of the high temperature in the case of a concentrator standalone PV cell, since the TEG can compensate for the decrease in the PV output power due to the decreased input power density of the limited spectrum. The PV-TEG system of configuration 1 has the highest overall efficiency, slightly higher than for a standalone PV cell. The PV cell temperature increases for each spectrum partition as the PV cell's concentration ratio increases from 2 to 5 suns. However, it can be seen that with increasing concentration levels, the temperature reduction effect of the splitting becomes more definite.

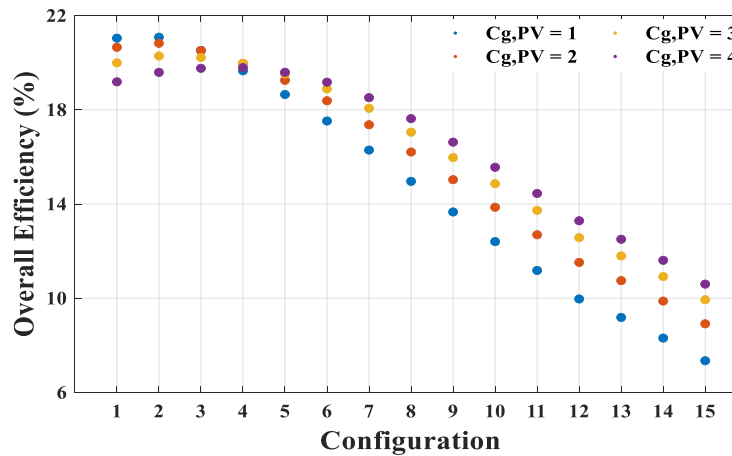
### **Proposed Spectrum Splitting at Higher Concentration**

At different PV concentration ratios, the PV cell efficiency decreases as the spectrum partition gets smaller due to the decrease in the input power density. It can also be seen that the efficiency of the PV cell decreases with concentration level when the entire within-bandgap spectrum, including the low wavelengths, is passed to the PV cell. However, by directing lower wavelength ranges (below 600 nm) to the TEG, the efficiency of the PV cell starts to increase with the light concentration level. This is due to the fact that at lower wavelengths, where the photons have significantly higher energy than the bandgap, a lot of excess heat is generated, and this heating effect is dominant over the light concentration's positive effect. However, at higher wavelengths, the photons with above-bandgap energy are much less, thus the heat load is significantly reduced, and the light concentration can exert its efficiency-increasing effect. Compared with the efficiencies of the standalone PV cell, in the case of 5 suns, the efficiency increases from 16.57 % to 18.509 %, albeit reducing the spectrum transferred to the PV cell by 50 nm (the 350-400 spectral range being redirected to the TEG). The overall output power increases significantly with the increase of the PV cell or TEG device concentration ratio. The maximum overall output power and efficiency at concentration ratios of 2, 3, and 4 suns were found to be at configuration 2. Whereas at 5 suns, configuration 4 showed the highest output, indicating a shift towards higher wavelengths in the optimal splitting wavelength with increasing concentration level (see Fig. 4.13 (a)). Comparing Figs.

4.13 (b) and 4.12 show that the proposed spectrum splitting principle demonstrates higher overall efficiency than that of the standalone PV cell, as summarized in Fig. 4.14. At higher concentrations, the hybrid system figures out more than a configuration that has higher efficiency than the standalone PV cell at the corresponding PV cell's concentration level. For example, at  $C_{g,PV} = 5$  suns and  $C_{g,TEG} = 255$  suns, the first nine configurations have higher efficiencies with the fourth configuration being the maximum, than that of the standalone PV cell at  $C_{g,PV} = 5$  suns. Moreover, higher concentration ratios demonstrate a higher efficiency of more configurations compared to the efficiency of the standalone PV cell. For example, as the concentration ratios increase from ( $C_{g,PV} = 1$  &  $C_{g,TEG} = 51$ ) to ( $C_{g,PV} = 4$  &  $C_{g,TEG} = 204$ ) suns, the first 5, 6, 7, and 8 configurations, respectively, have a higher efficiency than that of the standalone PV cell at a concentration ratio of  $C_{g,PV} = 5$  suns.



(a)



(b)

Fig. 4.13 Overall efficiency of the parallel hybrid system with (a) no concentration, and (b) concentration, for the 15 configurations.

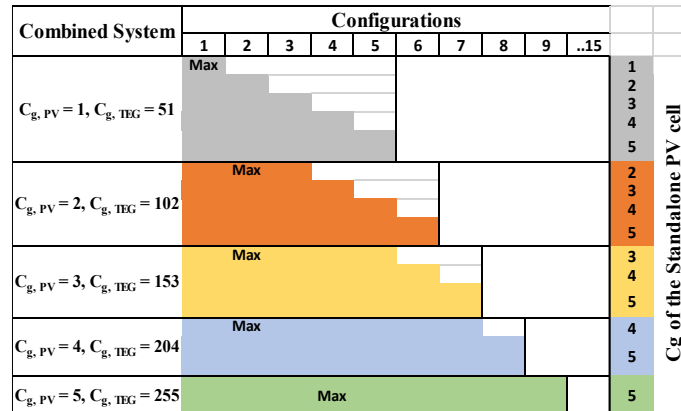


Fig. 4.14 Performance of the hybrid system against the standalone PV cell.

My contributions are summarized as follows

**Thesis 4** I have investigated and optimized a double spectrum-splitting concept for the parallel configuration to mitigate the limitations associated with post-bandgap and thermalization losses in standalone PV cells operating without active cooling mechanisms. The proposed spectrum-splitting approach directs the post-bandgap wavelength and a varying amount of the higher energy wavelength to the TEG. I have introduced fifteen distinct configurations of spectrum wavelength allocations, each analyzed through a thermal-electrical modeling framework.

**4.1** I have proved that the maximum overall efficiency shifts towards higher wavelengths with the light concentration level, being located at wavelength of 400 nm for  $C_{g,PV} = 1$  &  $C_{g,TEG} = 51$ , and at wavelength of 500 nm for  $C_{g,PV} = 5$  &  $C_{g,TEG} = 255$ .

**4.2** I have found that the optimum overall efficiency among the investigated light concentration levels is achieved at  $C_{g,PV} = 2$  &  $C_{g,TEG} = 102$ , which offers a trade-off between a moderate PV cell temperature of 334 K and an optimal splitting wavelength of 400 nm.

**4.3** I have demonstrated that the cutoff wavelength, at which the overall efficiency exceeds that of the standalone PV cell, increases with light concentration level. At  $C_{g,PV} = 2$  &  $C_{g,TEG} = 102$ , the cutoff wavelength is 450 nm (first three configurations), while at  $C_{g,PV} = 5$  &  $C_{g,TEG} = 255$ , it reaches 750 nm (first nine configurations).

**Related Publications:** The thesis's main concept has been published in [j3]. Some modeling concepts of the presented model have been published in [C3].

## Publications

### Publications Summary

Number of publications:	12
Number of peer-reviewed journal papers (written in English):	3
Number of articles in journals indexed by WOS or SCOPUS:	3
Number of publications with at least 50% contribution of the author:	12

Number of peer-reviewed publications:	12
Number of independent citations:	28

### Related Publications

	Journal Papers	Conferences and Workshops Papers
<b>Thesis I</b>	[j1]	[c5]
<b>Thesis II</b>	[j2]	[c1] [c3] [c4]
<b>Thesis III</b>	[j2]	[c2]
<b>Thesis IV</b>	[j3]	[c3]

### International Journals

[j1] Ahmed Issa Alnahhal and B. Plesz, "Extending the Single-Diode Model with Spectral Sensitivity for Different PV Materials Under Varying Solar Spectra." *Advanced Theory and Simulations* (2025): e01529. <https://doi.org/10.1002/adts.202501529>. (Q1, IF 2.9)

[j2] Ahmed Issa Alnahhal and B. Plesz, "Comparative assessments of configuration type and parameter optimization effects on the performance of a hybrid PV-TEG system," in *Energy Conversion and Management X*, 2025, <https://doi.org/10.1016/j.ecmx.2025.101428>. (D1, IF 7.6)

[j3] Ahmed Issa Alnahhal and B. Plesz, "Spectrum Splitting-Based Performance of Combined Photovoltaic Thermoelectric Generator System," in *IEEE Transactions on Components, Packaging and Manufacturing Technology*, vol. 14, no. 9, pp. 1560-1567, Sept. 2024, <https://doi.org/10.1109/TCPMT.2024.3446590>. (Q1, IF 3)

## **International Conferences**

[c1] Ahmed Issa Alnahhal, A. Halal and B. Plesz, "Model for Electricity Generation by Thermoelectric Generators used in Spectrum-Splitting Applications," *10th International Workshop on Teaching in Photovoltaics*, Prague, Czech Republic, 2022.

[c2] Ahmed Issa Alnahhal, A. Halal and B. Plesz, "Temperature-Dependent Performance of Concentrated Monocrystalline Silicon Solar Cell," *2022 22nd International Scientific Conference on Electric Power Engineering (EPE)*, Kouty nad Desnou, Czech Republic, 2022, pp. 1-6, <https://doi.org/10.1109/EPE54603.2022.9814124>.

[c3] Ahmed Issa Alnahhal, A. Halal and B. Plesz, "Thermal-Electrical Model of Concentrated Photovoltaic Thermoelectric Generator Combined System for Energy Generation," *2022 28th International Workshop on Thermal Investigations of ICs and Systems (THERMINIC)*, Dublin, Ireland, 2022, pp. 1-4, <https://doi.org/10.1109/THERMINIC57263.2022.9950655>.

[c4] Ahmed Issa Alnahhal and B. Plesz, "Performance Analysis of Stacked Photovoltaic-Thermoelectric Generator Using Mathematical Thermal-Electrical Model," *2023 29th International Workshop on Thermal Investigations of ICs and Systems (THERMINIC)*, Budapest, Hungary, 2023, pp. 1-5 <https://doi.org/10.1109/THERMINIC60375.2023.10325680>.

[c5] Ahmed Issa Alnahhal and B. Plesz, "Studying the Effect of Photon Wavelength on Solar Cell Efficiency," *2024 IEEE 7th International Conference and Workshop Óbuda on Electrical and Power Engineering (CANDO-EPE)*, Budapest, Hungary, 2024, pp. 000077-000082, <https://doi.org/10.1109/CANDO-EPE65072.2024.10772963>.

## **Other Publications**

[C6] A. Halal, A. I. Alnahhal and B. Plesz, "Numerical Simulation Based Physical Parameter Analysis of Perovskite/c-Si Tandem PV Cells," *10th International Workshop on Teaching in Photovoltaics*, Prague, Czech Republic, 2022.

[C7] A. Halal, A. I. Alnahhal and B. Plesz, "Numerical Simulation and Design Optimization of Highly Efficient Lead-free Perovskite/c-Si Tandem Solar Cell," *2022 22nd International Scientific Conference on Electric Power Engineering (EPE)*, Kouty nad Desnou, Czech Republic, 2022, pp. 1-6 <https://doi.org/10.1109/EPE54603.2022.9814136>

[C8] A. Halal, A. I. Alnahhal and B. Plesz, "Performance Analysis of Perovskite Solar Cell by Considering Temperature Effect on Physical Parameters of the Absorber Layer," *2022 28th International Workshop on Thermal Investigations of ICs and Systems (THERMINIC)*, Dublin, Ireland, 2022, pp. 1-4, <https://doi.org/10.1109/THERMINIC57263.2022.9950644>.

[c9] Mohammed A. Alhanjouri, Ahmed Issa Alnahhal Dc Motor Speed Control System Using Particle Swarm Optimization Technique *In: 5th International Conference on Engineering and Sustainability (ICES5)* (2014) p. 1

## References

- [1] P. Würfel and U. Würfel, *Physics of solar cells: from basic principles to advanced concepts*. John Wiley & Sons, 2016.
- [2] H. Jouhara *et al.*, “Thermoelectric generator (TEG) technologies and applications,” *Int. J. Thermofluids*, vol. 9, p. 100063, Feb. 2021, doi: 10.1016/j.ijft.2021.100063.
- [3] J. He and T. M. Tritt, “Advances in thermoelectric materials research: Looking back and moving forward,” *Science (80-. )*, vol. 357, no. 6358, Sep. 2017, doi: 10.1126/science.aak9997.
- [4] T. T. D. Tran and A. D. Smith, “Evaluation of renewable energy technologies and their potential for technical integration and cost-effective use within the U.S. energy sector,” *Renew. Sustain. Energy Rev.*, vol. 80, pp. 1372–1388, Dec. 2017, doi: 10.1016/j.rser.2017.05.228.
- [5] S. Brownsberger, N. Mondrik, and C. W. Stubbs, “Initial assessment of monocrystalline silicon solar cells as large-area sensors for precise flux calibration,” *J. Astron. Telesc. Instruments, Syst.*, vol. 6, no. 02, p. 1, Apr. 2020, doi: 10.1117/1.JATIS.6.2.026001.
- [6] B. M. Kayes *et al.*, “27.6% Conversion efficiency, a new record for single-junction solar cells under 1 sun illumination,” in *2011 37th IEEE Photovoltaic Specialists Conference*, Jun. 2011, pp. 000004–000008. doi: 10.1109/PVSC.2011.6185831.
- [7] V. Sorianello, L. Colace, C. Maragliano, D. Fulgoni, L. Nash, and G. Assanto, “Germanium-on-Glass solar cells: fabrication and characterization,” *Opt. Mater. Express*, vol. 3, no. 2, p. 216, Feb. 2013, doi: 10.1364/OME.3.000216.
- [8] X. Ju, Z. Wang, G. Flamant, P. Li, and W. Zhao, “Numerical analysis and optimization of a spectrum splitting concentration photovoltaic–thermoelectric hybrid system,” *Sol. Energy*, vol. 86, no. 6, pp. 1941–1954, Jun. 2012, doi: 10.1016/j.solener.2012.02.024.
- [9] D. A. Flores-Hernández, S. I. Palomino-Resendiz, N. Jost, and A. Luviano-Juárez, “Numerical energy evaluation of an optimized hybrid energy harvesting system (CPV-TEG) considering the effects of solar tracking,” *Appl. Therm. Eng.*, vol. 247, p. 123071, Jun. 2024, doi: 10.1016/j.applthermaleng.2024.123071.
- [10] B. Lorenzi and G. Chen, “Theoretical efficiency of hybrid solar thermoelectric-photovoltaic generators,” *J. Appl. Phys.*, vol. 124, no. 2, Jul. 2018, doi: 10.1063/1.5022569.
- [11] P. Li, L. Cai, P. Zhai, X. Tang, Q. Zhang, and M. Niino, “Design of a Concentration Solar Thermoelectric Generator,” *J. Electron. Mater.*, vol. 39, no. 9, pp. 1522–1530, Sep. 2010, doi: 10.1007/s11664-010-1279-0.
- [12] Z. Yang, W. Li, X. Chen, S. Su, G. Lin, and J. Chen, “Maximum efficiency and parametric optimum selection of a concentrated solar spectrum splitting photovoltaic cell-thermoelectric generator system,” *Energy Convers. Manag.*, vol. 174, pp. 65–71, Oct. 2018, doi: 10.1016/j.enconman.2018.08.038.
- [13] S. P. Cooperation, “MAXEON™ GEN III SOLAR CELLS Electrical Characteristics of a typical Maxeon Gen III Cell,” pp. 3–4, 2017.
- [14] Z. Li, W. Li, and Z. Chen, “Performance Analysis of Thermoelectric Based Automotive Waste Heat Recovery System with Nanofluid Coolant,” *Energies*, vol. 10, no. 10, p. 1489, Sep. 2017, doi: 10.3390/en10101489.
- [15] G. Li, X. Chen, and Y. Jin, “Analysis of the Primary Constraint Conditions of an Efficient Photovoltaic-Thermoelectric Hybrid System,” *Energies*, vol. 10, no. 1, p. 20, Dec. 2016, doi: 10.3390/en10010020.